NUMERICAL ANALYSIS OF VORTEX-VORTEX AND VORTEX-SHOCK INTERACTIONS AT HYBRID-DELTA-WING CONFIGURATIONS

Y. Özdemir*, C. Breitsamter*
* Technical University of Munich, Chair of Aerodynamics and Fluid Mechanics, Boltzmannstr. 15, 85748 Garching, Germany

Abstract

This study examines the vortex-dominated flow field around triple-delta and double-delta-wing configurations under transonic flow conditions, with an emphasis on vortex-vortex and vortex-shock interactions. In this regard, numerical simulations were conducted at Mach numbers of 0.75, 0.85, and 0.95 for an angle of attack range of $16° \leq \alpha \leq 32°$. Validation against the experimental data reveals that scale-resolving simulations provide improved accuracy, particularly at high incidence angles. Inboard vortex breakdown occurs further downstream with increasing Mach number at $\alpha = 16°$. At a Mach number of 0.85, two normal shocks form on the triple-delta wing, whereas a single shock forms on the double-delta wing at $\alpha = 16°$. The inboard vortex of the triple-delta wing undergoes breakdown upon interacting with the second shock at $\alpha = 16°$, while it bursts upstream of the shock at $\alpha = 24°$. In contrast, a more robust inboard vortex develops on the double-delta wing, and it does not burst at $\alpha = 16°$ and $\alpha = 24°$ on the wing despite the shock. Finally, sideslip conditions result in a more intense vortex system on the windward side, bursting abruptly and causing asymmetric lift generation at $\alpha = 24°$. This roll reversal is captured in the numerical results for both configurations.

Keywords

Multi-Swept Delta Wing; Vortical Flow; Vortex-Vortex Interaction; Vortex-Shock Interaction

NOMENCLATURE

Symbols

a	Speed of sound	$[\mathrm{m/s}]$
α	Angle of attack	$[°]$
Λ	Aspect ratio	[-]
β	Angle of sideslip	$[°]$
C_L	Lift coefficient	[-]
C_{mx}	Rolling moment coefficient	[-]
C_{my}	Pitching moment coefficient	[-]
$C_{my\alpha}$	Pitching moment derivative	[-]
C_{mz}	Yawing moment coefficient	[-]
C_p	Pressure coefficient	[-]
c_r	Root chord length	$[\mathrm{m}]$
δ	Axial velocity deficit	[-]
Δt	Physical time-step size	$[\mathrm{s}]$
l_μ	Mean aerodynamic chord	$[\mathrm{m}]$
Ma	Mach number	[-]
φ	Sweep angle	$[°]$
Q	Q-Criterion	$[1/\mathrm{s}^2]$
Re	Reynolds number	[-]
Ro	Rossby number	[-]
s	Half span	$[\mathrm{m}]$
U_∞	Freestream velocity	$[\mathrm{m/s}]$
u_x	Axial velocity	$[\mathrm{m/s}]$
$U_{\theta,max}$	Maximum tangential velocity	$[\mathrm{m/s}]$
x, y, z	Body-fixed cartesian coordinates	[-]

Acronyms

AVT	Applied vehicle technologies
DLR	German aerospace center
FV	Forebody vortex
IBV	Inboard vortex
IDDES	Improved delayed detached eddy simulation
LER	Leading-edge radius
LES	Large eddy simulation
LEVCON	Leading-edge vortex controller
LEV	Leading-edge vortex
MBV	Midboard vortex
NA1_W1	Baseline triple-delta-wing configuration
NA1_W2	Baseline double-delta-wing configuration
NATO	North Atlantic Treaty Organization
URANS	Unsteady Reynolds-Averaged-Navier-Stokes
VFE	Vortex flow experiment
WT	Wind tunnel

doi: 10.25967/650316

1. INTRODUCTION

The flight envelope of modern high-agility aircraft covers a wide range of extreme flight conditions. They are designed to operate supersonic cruise as efficiently as possible, while maintaining high maneuverability in the sub- and transonic flow regimes [1]. To fulfill these requirements for more advanced aerodynamic characteristics, military aviation has adopted low-aspect-ratio wing planforms featuring medium to high sweep angles and a small leading edge, known as delta wings. Leading-edge vortices (LEV) dominate the flow topology over such wing planforms. Accordingly, the flow separates at the sharp leading edge already at moderate angles of attack α, and the separating shear layer on both wing sides rolls up to form the primary vortices. The LEVs induce additional suction on the wing surface, providing a nonlinear lift contribution and smoother post-stall flight characteristics, an essential feature for complex maneuvers [2]. Increasing the angle of attack intensifies the vortex strength; however, once the critical angle is exceeded, the vortex size suddenly grows, and the velocity field exhibits large-scale fluctuations. This rapid distortion of the vortex topology is known as vortex breakdown [3].

Modern high-agility aircraft utilize multi-swept delta wing or strake-wing configurations featuring different leading-edge sweep angles φ. At such configurations, multiple vortices form and may interact with each other. Besides, normal shocks occur at transonic flow speeds, interacting with the vortex system. Therefore, it is significant to investigate these vortex-vortex and vortex-shock interactions for the design of the modern combat aircraft.

Flow field and flight stability characteristics for a variety of double-delta and triple-delta-wing configurations, comparable to those of the present study, were investigated at the Chair of Aerodynamics and Fluid Mechanics at the Technical University of Munich [4] [5] [6] [7]. Accordingly, the distinctive flow structures are the Inboard Vortex (IBV) and the Midboard Vortex (MBV). The IBV forms at the non-slender section of the triple-delta wing, whereas it develops at the slender strake segment of the double-delta wing. Hence, the IBV of the double-delta wing breaks down at higher angles of attack, yet the vortex breakdown occurs abruptly, which causes the MBV to burst, as well. On the other hand, the IBV of the triple-delta-wing configuration displays a smoother bursting characteristic featuring less velocity fluctuations; consequently, the stability of the MBV is not impaired drastically in contrast to the double-delta-wing configuration [4]. The influence of leading-edge radius (LER) was investigated by Sedlacek and Breitsamter for double-delta and triple-delta-wing configurations. It was observed that increasing LER delays the onset of the vortex breakdown for the double-delta-wing configuration, whereas the triple-delta-wing configuration displayed a more LER-insensitive vortex system [7].

The increasing computational power over time has enabled the use of Computational Fluid Dynamics (CFD) simulations during the design of high-performance aircraft. The First International Vortex Flow Experiment (VFE-1) [8] was initiated to evaluate the capability of the Euler codes available at the time. Due to the lack of modeling of the secondary separation, the codes were inadequate to depict the flow field despite the fixed primary vortex formation. As a successor to this campaign, VFE-2 [9] was initiated to provide the necessary experimental data to assess the progress in numerical methods for calculating vortical flows. Schiavetta et al. [10] investigated a 65° single-delta wing and observed a sudden change in the vortex breakdown location with an increase in the angle of attack under transonic freestream conditions. However, numerical results show an earlier onset of vortex breakdown compared to the experimental data, posing another challenge for the computational approach to overcome. Further investigations were conducted within the Cranked Arrow Wing Aerodynamics Project (CAWAP) [11], focusing on an F-16XL configuration with a comparable wing configuration to the triple-delta-wing configuration of the present study at subsonic and transonic freestream flow regimes. Hitzel [1] found a weak crossflow shock interacting with the inboard vortex, while the outboard wing vortex interacts with the normal shock strongly at a medium angle of attack. At a higher incidence angle, more intense vortex-shock interactions are reported. Within the scope of NATO-AVT 316 research group, where the geometries of the present work are of interest, Sedlacek et al. [5] provided flow field analysis for subsonic flow conditions at Mach number (Ma) of 0.15, while Russel et al. [12] reported their findings at $Ma = 0.50$ and 0.85. In this project, Werner et al. [13] compared different turbulence models at $Ma = 0.50$ and 0.85 for a triple-delta-wing configuration. Menter SST yielded the closest results to the experimental data. Hövelmann et al. [14] investigated the same triple-delta-wing configuration at $Ma = 0.85$. The impact of vortex-shock interactions on vortex breakdown was demonstrated, and consequently, how the longitudinal and lateral flight characteristics were impaired. Werner et al. [15] investigated another generic multi-swept delta wing configuration featuring sweep angles of 45°, 74°, and 45° within the scope of the DLR Diabolo project at $Ma = 0.50,\ 0.85,\ 1.10,$ and 1.41. It was observed that vortex-shock interaction occurs at $Ma = 0.85$ above the wing, and it causes shock-induced vortex breakdown at $\alpha = 16^\circ$, whereas for higher angles of attack, vortex breakdown occurs upstream of the shock. It was also noted that the swirling ratio increases suddenly above the critical value as a result of the vortex-shock interaction. Di Fabbio et al. [16] [17] [18] investigated the flow field around a slender delta wing and a triple-delta wing numerically at $Ma = 0.80$ and 0.85, respectively. It is concluded that the state of the secondary vortex impacts the susceptibility of the inboard vortex to shock-induced breakdown. The turbulent flow structures resulting from secondary vortex breakdown block the shear layer feeding the primary vortex. Consequently, the primary vortex weakens and becomes more vulnerable to the consequences of interacting with the shock [18].

The objective of this study is to provide a flow field description for various transonic flow speeds and angles of attack using two multi-swept generic wing-fuselage configurations, a triple-delta wing and a double-delta wing, at various Ma and α values for both symmetric and asymmetric inflow conditions. Thereby, vortex-shock interactions and consequences of such interactions on the longitudinal and lateral flight characteristics are the main points of this present study.

2. CONFIGURATIONS

Two generic multi-swept delta wing-fuselage configurations are investigated in this study. The triple-delta-wing configuration, NA1_W1, is shown on the left-hand side and the double-delta-wing configuration, NA1_W2, on the right-hand side of Figure 1 [5]. The NA1_W1 configuration is equipped with a Leading-Edge Vortex Controller segment (LEVCON) featuring a sweep angle of $\varphi_1 = 52.5^\circ$. The LEVCON is followed by a strake section characterized by

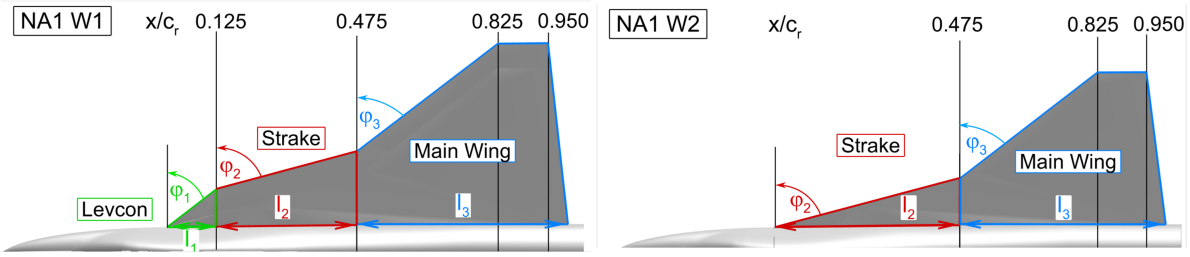

FIG 1. Multi-swept delta wing planforms [5].

a high leading-edge sweep angle of $\varphi_2 = 75°$ and a main wing section featuring $\varphi_3 = 52.5°$. The NA1_W2 configuration, on the other hand, is characterized by a highly swept strake and a moderately swept main wing element with the same φ_2 and φ_3 as the NA1_W1 configuration. These configurations have sharp leading edges and consist of flat plates. The significant geometric parameters for both configurations are given in Table 1 [4].

TAB 1. Geometric parameters of the NA1_W1 and NA1_W2 configurations [4].

Parameter	NA1_W1	NA1_W2
c_r [m]	0.802	0.802
s [m]	0.417	0.367
S_{ref} [m^2]	0.329	0.266
Λ [-]	2.11	2.03
l_μ [m]	0.468	0.426
l_1/c_r [-]	0.125	-
l_2/c_r [-]	0.350	0.475
l_3/c_r [-]	0.475	0.475
φ_1 [°]	52.5	-
φ_2 [°]	75	75
φ_3 [°]	52.5	52.5

3. NUMERICAL APPROACH

3.1. Grid

This project utilizes the computational grids generated during the previous studies with the mesh generator Centaursoft, as shown in Figure 2 [6]. During the mesh generation procedure, the aim was to maintain similar grid structures for both configurations. Grid independence studies were conducted for both numerical grids; consequently, grids consisting of $52 \cdot 10^6$ elements were employed throughout the project. Further details regarding the grid generation and grid independence studies are shown in detail by Sedlacek et al. [5], [6], [19]. In this section, the meshing procedure is briefly described for a complete depiction of the numerical methods used in this project.

The spherical computational domain has a diameter of 50 times the model size to diminish the impact of the far-field region, the outer region of the domain, on the flow field. The viscous wall boundary condition is attained for the surfaces. For an adequate resolution of the boundary layer, 33 prism layers are generated with a stretching ratio of 1.25 based on the unstructured surface grid consisting of tetrahedral elements. Each region has different grid element sizes, and grids in the critical regions with high gradients are refined further. Although the unstructured elements are the main cell shape, a block of structured hexahedral elements is generated above the wing to capture the vortex-dominated flow field more accurately. Pyramid elements fill the space between the hexahedra and tetrahedra.

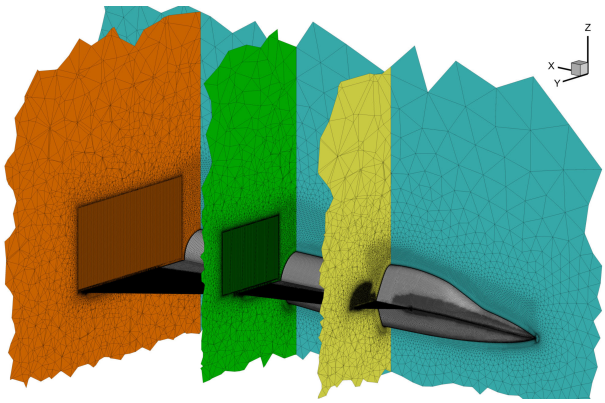

FIG 2. Overview of the computational grid [6].

3.2. Applied Numerical Setup and Flow Conditions

The numerical simulations for this project were conducted using the DLR TAU Code, a three-dimensional solver based on the Finite Volume Method developed by the German Aerospace Center (DLR).

Time-accurate unsteady Reynolds-Averaged-Navier-Stokes (URANS) computations are performed using a dual-time stepping approach in combination with the lower-upper-symmetric Gauss-Seidel method. The spatial discretization is done utilizing the second-order central scheme with matrix dissipation. Turbulence is modeled by employing the one-equation Spalart-Allmaras model [20] in its negative formulation [21] with rotation correction (SARC-neg) [22]. The physical time-step size Δt is set to $2 \cdot 10^{-4}$ s. The convergence of the inner iterations is evaluated based on user-defined Cauchy convergence criteria, which require the relative change in lift, drag, and pitching moment coefficients to remain below $1 \cdot 10^{-4}$ for the last 20 samples. Besides, the number of inner iterations per time step is limited to 50-600. A secondary grid is generated based on the primary grid using a cell-vertex grid metric, enabling users to employ a multigrid approach to accelerate the convergence behavior of the simulations.

For higher fidelity, Improved Delayed Detached Eddy Simulation (IDDES) computations were performed based on the URANS results. Detached Eddy Simulation (DES) is a hybrid method proposed by Spalart et al. [23] that offers higher fidelity at an affordable computational cost. This method employs RANS in the near-wall region to model the small-scale flow structures, whereas large-scale turbulent flow structures in the detached flow regions are resolved using the Large Eddy Simulation (LES) method. In some cases, the transition to LES in the boundary layer region cannot be avoided; therefore, Spalart et al. [24] introduced the Delayed Detached Eddy Simulation (DDES), a modification that ensures the use of RANS in the boundary layer. IDDES is another modification proposed by Shur et al. [25], combining DDES and the wall-modeling LES branch. A time-step sensitivity study for IDDES computations is carried out, and it is found that $\Delta t = 2 \cdot 10^{-5}\,\mathrm{s}$ provides the best compromise between accuracy and computational cost, as shown in Section 4.1. In contrast to URANS computations, the second-order central scheme is employed with scalar dissipation to improve the stability of the simulations. The minimum number of inner iterations per time step is set to 30; however, the same Cauchy convergence criteria are used for IDDES computations. Simulations are carried out at transonic freestream velocities, namely at $Ma = 0.75,\ 0.85,$ and 0.95. Re for $Ma = 0.85$ case is defined as $1.20 \cdot 10^7$ for comparability with the experimental data provided by DLR and Airbus Defense and Space. For other flow conditions, Re calculation is done by maintaining the thermodynamic conditions the same as for flow at $Ma = 0.85$. Consequently, Re values of $1.06 \cdot 10^7$ and $1.34 \cdot 10^7$ are used for $Ma = 0.75$ and 0.95, respectively. The angle of attack range $\alpha \in [16^\circ, 32^\circ]$ is considered in this study. URANS computations are carried out with an increment of 4°, while high-fidelity simulations are performed for an increment of 8°. This α range is simulated for both symmetric and asymmetric flow conditions by setting the angle of sideslip (β) to 0° and 5°, respectively.

4. RESULTS AND DISCUSSION

This section presents numerical results for both triple-delta and double-delta-wing configurations. Firstly, the URANS and IDDES results for NA1_W1 configuration at $Ma = 0.85$ are compared to the experimental data. After the applied numerical setup is assessed, the flow physics at different flight conditions, as well as vortex-vortex and vortex-shock interactions, are investigated in detail for both sideslip angles.

4.1. Time-Step Sensitivity Study

High-angle-of-attack flow over a multi-swept delta wing features a complex unsteady vortex system with instabilities such as shear-layer and vortex-breakdown oscillations [26]. Temporal discretization is a significant parameter influencing the resolution level of such unsteady flow phenomena; hence, a time-step sensitivity study is conducted using the IDDES method with $\Delta t = 2 \cdot 10^{-4}\,\mathrm{s}, 2 \cdot 10^{-5}\,\mathrm{s}, 1 \cdot 10^{-5}\,\mathrm{s}, 5 \cdot 10^{-6}\,\mathrm{s}$, and $2 \cdot 10^{-6}\,\mathrm{s}$, corresponding to range of dimensionless steps $\Delta t^* \equiv \Delta t U_\infty / l_\mu$ of $[0.126 - 0.00126]$. The triple-delta wing is analyzed at $Ma = 0.85$, $\alpha = 16^\circ$ due to the presence of vortex-shock interactions.

Figure 3 demonstrates the surface pressure coefficient (C_p) plots obtained for $\Delta t = 2 \cdot 10^{-4}\,\mathrm{s},\ 2 \cdot 10^{-5}\,\mathrm{s},$ and $2 \cdot 10^{-6}\,\mathrm{s}$ alongside the wind tunnel (WT) data. The distinctive flow features of the selected flow condition are two normal shocks, characterized by a sudden pressure increase on the surface, and their interaction with vortices. The first shock forming downstream of the LEVCON–strake junction is accurately predicted, while $\Delta t = 2 \cdot 10^{-4}\,\mathrm{s}$ yields overestimated pressures in its wake due to the weaker IBV. WT data indicate the MBV development along the leading edge until the second shock, causing a lower negative pressure on the surface compared to the numerical results. Simulations with $\Delta t \leq 2 \cdot 10^{-5}\,\mathrm{s}$ predict the second shock slightly downstream of the WT location, and a stronger MBV-induced suction. In contrast, $\Delta t = 2 \cdot 10^{-4}\,\mathrm{s}$ underpredicts suction and misplaces the shocks. Accordingly, $\Delta t = 2 \cdot 10^{-5}\,\mathrm{s}$ is employed for IDDES computations in this project; further refinement of the temporal discretization does not significantly alter the results, as both the shock locations and the vortex-induced suction remain unchanged.

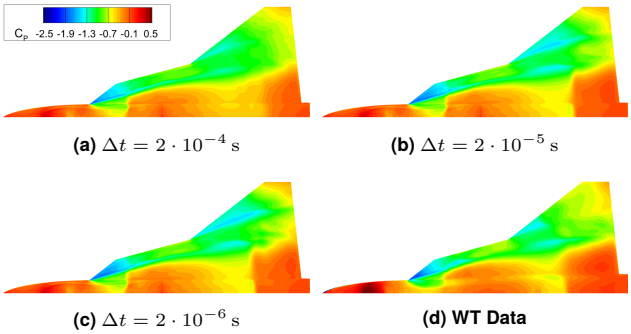

(a) $\Delta t = 2 \cdot 10^{-4}\,\mathrm{s}$ **(b)** $\Delta t = 2 \cdot 10^{-5}\,\mathrm{s}$

(c) $\Delta t = 2 \cdot 10^{-6}\,\mathrm{s}$ **(d) WT Data**

FIG 3. Comparison of surface pressure distribution plots for different Δt values with experimental data.

4.2. Assessment of Numerical Results with Wind-Tunnel Data

In this section, IDDES results are evaluated against the WT data, and the improvements over the URANS simulations is examined through the C_p plots. Figure 4 illustrates the surface pressure distribution of the numerical results and the experimental data at $\alpha = 16^\circ$. URANS significantly overestimates the suction induced by the IBV on the LEVCON segment. The first shock occurs slightly downstream of the LEVCON-strake junction, as indicated by the sudden pressure increase, and is well captured compared to the experimental data. However, the deficiency of the URANS to capture the reduction in suction level after the shock, in contrast to the IDDES, is observed. Both simulations overpredict the suction generated by the MBV along the leading edge of the main wing. The position of the second shock is numerically predicted slightly further downstream than in the experiment. Both methods show a vortex-shock interaction, with URANS producing a sharp pressure rise along the IBV path, while IDDES predicts a smoother reduction in suction, closer to the measurements.

IDDES predicts a more gradual decrease in the IBV-induced suction level on the LEVCON segment at $\alpha = 24^\circ$, in agreement with the WT data; however, it cannot fully represent the suction level attenuation on the strake section, see Figure 5b and 5c. On the other hand, URANS overestimates the IBV strength, as shown in Figure 5a. The deficiency of the numerical results is notable regarding the MBV formation. Experimental data reveal no imprint of the MBV, whereas numerical results display the suction footprint of the MBV; however, URANS shows higher inaccuracy in this case. The position and strength of the second shock could not be predicted by IDDES with sufficient accuracy relative to the ex-

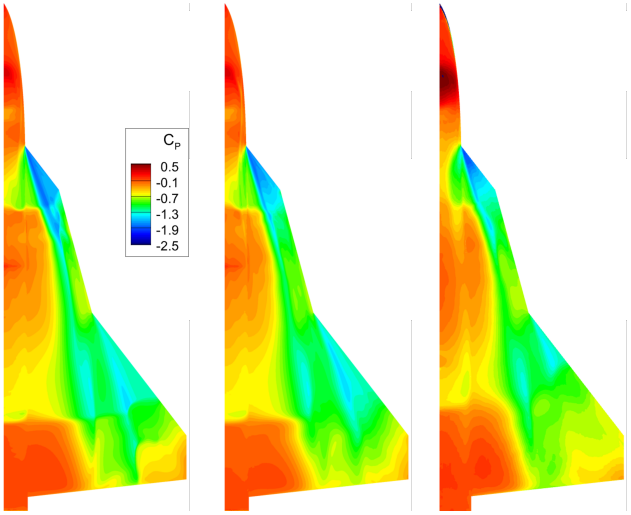

(a) URANS ($\alpha = 16°$) **(b) IDDES ($\alpha = 16°$)** **(c) WT ($\alpha = 16°$)**

FIG 4. Surface pressure distribution plots of the numerical results and the experimental data at $Ma = 0.85$ & $Re = 1.20 \cdot 10^7$, $\alpha = 16°$ & $\beta = 0°$.

periment. URANS, in contrast, produces a sharp pressure increase indicating a strong shock, which causes the highly stable IBV to burst upon interaction.

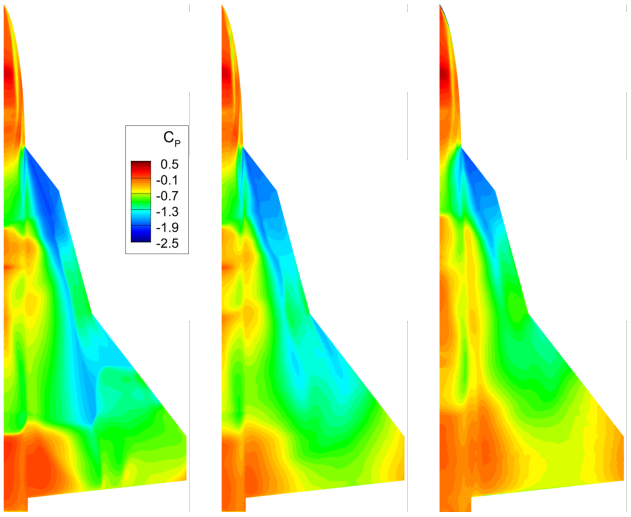

(a) URANS ($\alpha = 24°$) **(b) IDDES ($\alpha = 24°$)** **(c) WT ($\alpha = 24°$)**

FIG 5. Surface pressure distribution plots of the numerical results and the experimental data at $Ma = 0.85$ & $Re = 1.20 \cdot 10^7$, $\alpha = 24°$ & $\beta = 0°$.

Vortex breakdown has already reached the apex at $\alpha = 32°$ during the wind tunnel measurements, which is accurately reproduced by IDDES, see Figure 6b and 6c. However, URANS inaccurately depicts the flow field on the LEVCON, predicting the formation of IBV, as shown in Figure 6a. Overall, numerical results yield similar flow field descriptions at $\alpha = 16°$. However, at higher incidence angles, IDDES provides improvements in the accuracy of the simulations, despite deficiencies at $\alpha = 24°$.

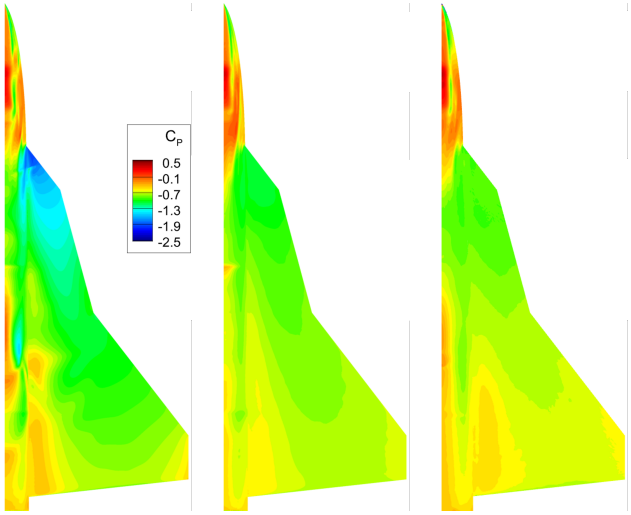

(a) URANS ($\alpha = 32°$) **(b) IDDES ($\alpha = 32°$)** **(c) WT ($\alpha = 32°$)**

FIG 6. Surface pressure distribution plots of the numerical results and the experimental data at $Ma = 0.85$ & $Re = 1.20 \cdot 10^7$, $\alpha = 32°$ & $\beta = 0°$.

4.3. Flow Field Analysis at $\beta = 0°$

4.3.1. Effect of Mach Number

This section analyzes vortex-vortex and vortex-shock interactions under symmetric flow conditions. For this purpose, the effect of Ma, α, and the wing geometry is investigated. An overview of the vortex-dominated flow field is presented for $Ma = 0.75$, 0.85, and 0.95 at $\alpha = 16°$ around the NA1_W1 configuration in Figure 7. The topology of the IBV becomes flatter with an increasing Ma, and this spanwise elongation of the IBV is especially visible at $Ma = 0.95$, as shown in Figure 7c. The secondary vortex formation is more pronounced at $Ma = 0.75$ along the LEVCON-leading edge. Upon reaching the strake section, a reduction in the axial vorticity level and the enlargement of the vortex size are observed for all cases, attributable to the pressure increase and the disrupted secondary vortex as explained by Di Fabbio et al. [16]. Accordingly, the secondary vortex cannot be sustained downstream of the LEVCON and breaks down. The resulting turbulent flow structures block the feeding mechanism of the primary vortex from the shear layer. The disruptive influence of the secondary vortex increases with increasing Ma.

The MBV forms at the apex of the main wing, and similar trends in vortex size with increasing freestream Ma are observed. For all cases, the MBV features a distinct core of vorticity and shows no sign of vortex breakdown, although the level of axial vorticity reduces in the freestream direction. At $Ma = 0.75$ and 0.85, the MBV gains vorticity along the swept part of the main wing, whereas the cranked edge also feeds the MBV at $Ma = 0.95$. The comparison of Figure 7a and 7c also demonstrates that increasing freestream velocity reduces the deflection of a vortex in its flow direction. Forebody vortices (FV) are present for all Ma cases, yet they are more prominent at $Ma = 0.95$, where they are still visible over the main wing and curl under the IBV.

Leading-edge vortices are represented using the iso-surfaces of the Q-Criterion (Q) for the analysis of the vortex-vortex and vortex-shock interactions. This parameter describes a vortex as a connected fluid region with a positive second invariant of velocity gradient $\nabla \mathbf{u}$, and is

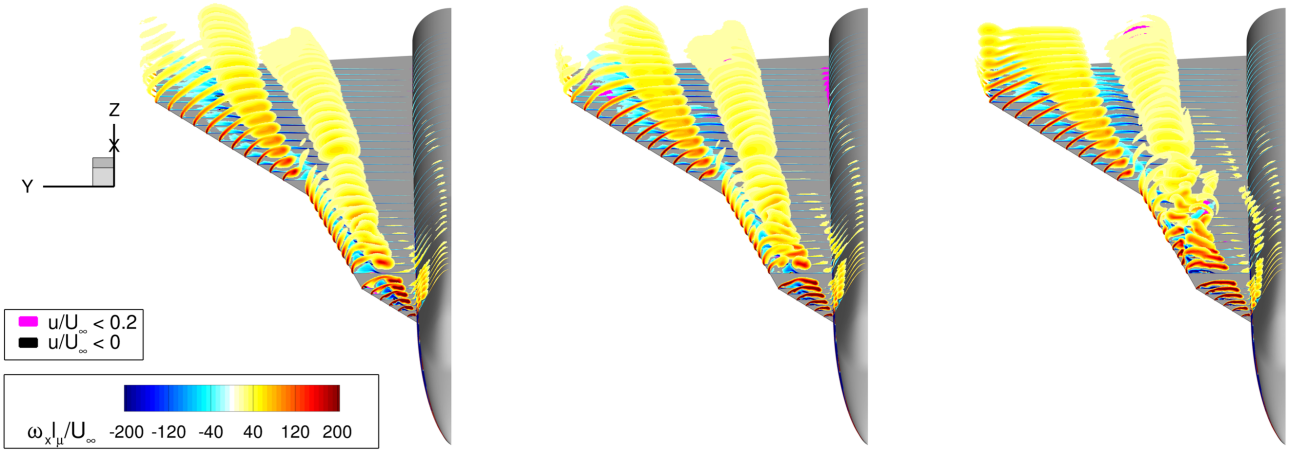

(a) $Ma = 0.75$ & $Re = 1.06 \cdot 10^7$ **(b)** $Ma = 0.85$ & $Re = 1.20 \cdot 10^7$ **(c)** $Ma = 0.95$ & $Re = 1.34 \cdot 10^7$

FIG 7. Overview of the axial vorticity at different slices for NA1_W1 at $\alpha = 16°$.

defined by Eq. (1), where $\mathbf{\Omega}$ represents the vorticity tensor and $\mathbf{S}$ stands for the strain-rate tensor [27].

$$Q = \frac{1}{2}\left(\|\mathbf{\Omega}\|^2 - \|\mathbf{S}\|^2\right) > 0 \tag{1}$$

Figure 8 illustrates the isosurfaces of the non-dimensional Q-Criterion, $Q^* = Q{l_\mu}^2/U_\infty^2 = 50$, colored by local Ma for $Ma = 0.75,\ 0.85,$ and 0.95 at $\alpha = 16°$. Besides, the shock surface feature of Tecplot [28] is utilized to demonstrate the vortex-shock interactions, where U_∞ is the freestream velocity, a is the speed of sound, and $\nabla p/\|\nabla p\|$ is the unit vector of the pressure gradient.

$$\frac{U_\infty}{a} \cdot \frac{\nabla p}{\|\nabla p\|} \tag{2}$$

Regions of this parameter being equal to 1 are visualized alongside the vortical structures.

The IBV and the MBV are traced to extract the vortex core data for a more elaborate investigation of the flow field. For this purpose, the maximum Q is searched by an algorithm in a 2D cross-section to locate the vortex core location, where the longitudinal and transversal data are extracted. Based on the vortex core data, Rossby number (Ro) and axial velocity deficit (δ) are calculated, as defined by Eq.(3) and Eq.(4), respectively.

$$Ro = \frac{u_x}{U_{\theta,max}} \tag{3}$$

$$\delta = 1 - \frac{u_x}{U_\infty} \tag{4}$$

Ro is the ratio of the axial velocity to the maximum tangential velocity of a vortex. This parameter is related to the vortex strength, and Robinson et al. [29] defined 1.4 as the limit of a stable vortex, whereas the region between 0.9 and 1.4 was identified as the unstable region, below which vortex bursts. If $\delta < 0$, then $u/U_\infty > 1$ shows the presence of a jet-type vortex, whereas $\delta > 0$ indicates a wake-type vortex. Figure 9 reveals the Ro and δ plots for the IBV of the triple-delta-wing configuration in the axial direction for $Ma = 0.75,\ 0.85,$ and 0.95 at $\alpha = 16°$. Additionally, $\alpha = 24°$ is shown for $Ma = 0.85$.

At $Ma = 0.75$, no normal shock occurs, but a crossflow shock is present in the vicinity of the LEVCON-leading-edge. The crossflow shock becomes more evident with increasing Ma, and this may disrupt the secondary vortex. The destabilization of the flow field mentioned above can also be seen in Figure 9b, where a positive δ indicates the transition from a jet-type to wake-type vortex in the strake region, which is accompanied by a decrease in Ro between $x/c_r = 0.2$ and 0.3, see Figure 9a. As mentioned earlier, this interaction is more intense for high Ma inflow conditions. For all Ma cases at $\alpha = 16°$, the IBV gets energized along the strake, which is observable through negative δ values. At $Ma = 0.75$, a decrease in local Ma and the Q^* size of the IBV indicates the breakdown at $x/c_r = 0.75$, while the IBV displays a jet-type characteristic until the complete break-

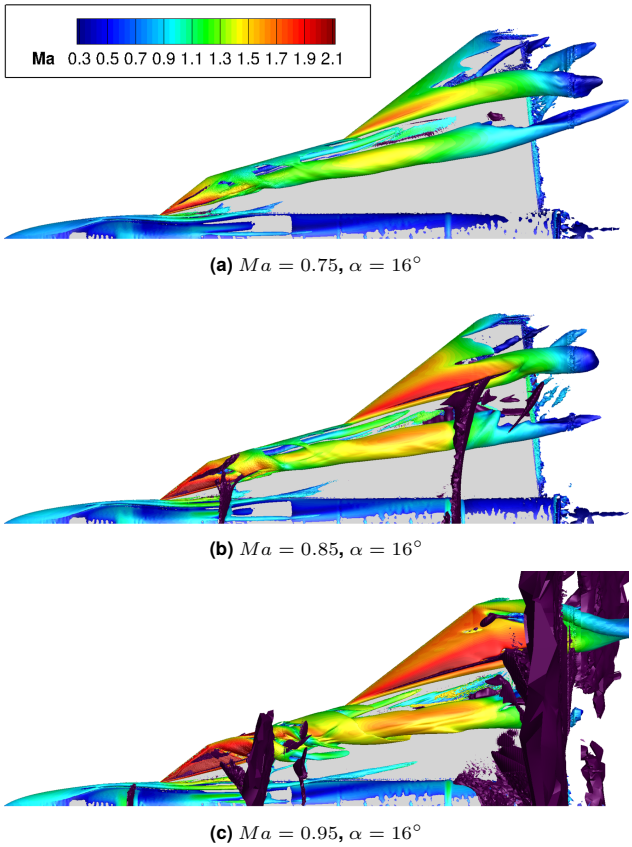

(a) $Ma = 0.75$, $\alpha = 16°$

(b) $Ma = 0.85$, $\alpha = 16°$

(c) $Ma = 0.95$, $\alpha = 16°$

FIG 8. Isosurfaces of the non-dimensional Q-Criterion of 50 for the triple-delta-wing configuration at $Ma = 0.75$ & $Re = 1.06 \cdot 10^7$; $Ma = 0.85$ & $Re = 1.20 \cdot 10^7$; and $Ma = 0.95$ & $Re = 1.34 \cdot 10^7$, $\alpha = 16°$ & $\beta = 0°$.

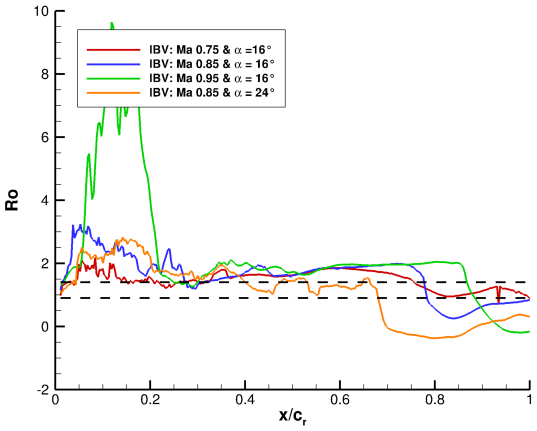

(a) Rossby number variation

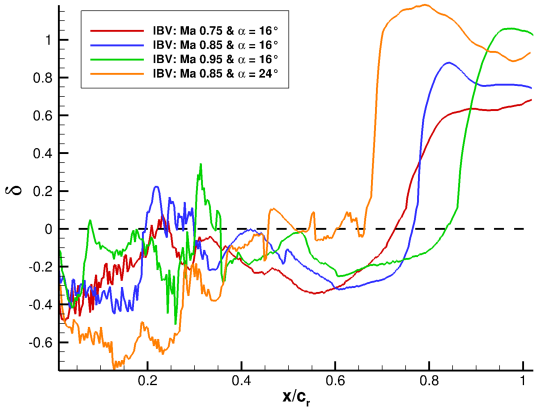

(b) Axial velocity deficit variation

FIG 9. Inboard vortex core characteristics of the triple-delta-wing configuration.

down occurs. Although Ro does not fall below the critical value of 0.9, it is still in the interval of instability. On the other hand, the MBV features still have high flow velocities. At around $x/c_r = 0.77$, the second shock occurs at $Ma = 0.85$, and this causes a sharp reduction in local Ma and contraction of the IBV, whereas this interaction mildly impacts the MBV, see Figure 8b. This vortex-shock interaction is visible through a sudden decrease in Ro below the critical value, accompanied by a transition to a wake-type vortex. At $Ma = 0.95$, the second shock occurs directly at the trailing edge, yet the IBV bursts at $x/c_r = 0.86$, characterized by a sharp decrease in Ro below the critical value, accompanied by a sign change of δ. Similar to the other Ma cases, the MBV shows no sign of vortex breakdown.

4.3.2. Effect of the Angle of Attack

Higher incidence angles generally enhance the circulation of the vortex; consequently, also the strength of the vortex. However, the stability of the vortex is inversely proportional to the strength. Hence, once a critical angle of attack is reached, the vortex breaks down [3]. The influence of the incidence angle is investigated for the triple-delta-wing configuration at $Ma = 0.85$. Figure 10a illustrates a more pronounced and voluminous IBV formation, featuring higher local Ma at $\alpha = 24°$. The shock does not spread across the whole span, but rather interacts with the forebody vortex. Complete breakdown of the IBV is illustrated in Figure 9 at around $x/c_r = 0.67$. Further increase in the angle of attack to $\alpha = 32°$ causes the leading-edge vortices to break down at the apex, which can be identified by the absence of coherent $Q^* = 50$ isosurface for both the IBV and the MBV, as shown in Figure 10b.

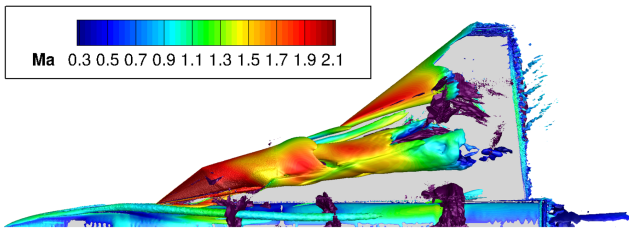

(a) $Ma = 0.85$, $\alpha = 24°$

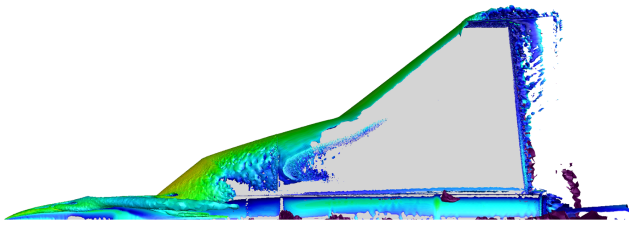

(b) $Ma = 0.85$, $\alpha = 32°$

FIG 10. Isosurfaces of the non-dimensional Q-Criterion of 50 for the triple-delta-wing configuration at $Ma = 0.85$ & $Re = 1.20 \cdot 10^7$, $\alpha = 24°$ and $32°$ & $\beta = 0°$.

4.3.3. Effect of the Wing Geometry

To assess the influence of the wing geometry, the flow topologies of the double-delta and triple-delta-wing configurations are compared. Figure 11 illustrates the evolution of the leading-edge vortices on the double-delta-wing configuration at $\alpha = 16°$, $24°$, and $32°$ for $Ma = 0.85$. The IBV formation starts at the apex of the highly swept strake section of the configuration and exhibits a more robust structure. As Figure 11a reveals, one shock occurs above the main wing in contrast to the flow field around the triple-delta wing. The IBV is fed along the entire strake leading edge and exhibits high local Ma values, exceeding 1.5, until it encounters the shock. The interaction with the shock causes the local Ma to drop; however, the IBV does not show any sign of vortex breakdown over the wing. The MBV, on the other hand, gains vorticity partially along the main wing, possibly due to the presence of the cross-shock, and the local Ma reduces sharply after interacting with the normal shock despite high flow velocities upstream of the shock, which indicates the breakdown of the MBV. At $\alpha = 24°$, the IBV grows in size and exhibits even higher flow velocities, and the interaction with the shock reduces the local Ma to around 1.4. The MBV directly deflects inward and interacts with the IBV after interacting with the shock. At $\alpha = 32°$, in contrast to the triple-delta-wing configuration, the IBV forms and is fed along a significant portion of the strake leading edge, as indicated by the presence of a $Q^* = 50$ isosurface. Thus, it can be concluded that the IBV breakdown has not yet reached the apex. On the other hand, a weak $Q^* = 50$ isosurface is visible on the main wing, indicating the MBV breakdown has reached the vicinity of the main wing kink.

4.4. Flow Field Analysis at $\beta = 5°$

In this section, the flow field is investigated for asymmetric inflow conditions at $\beta = 5°$. In this regard, IDDES and URANS results are evaluated based on the experimental data for the triple-delta-wing configuration at $Ma = 0.85$, followed by a

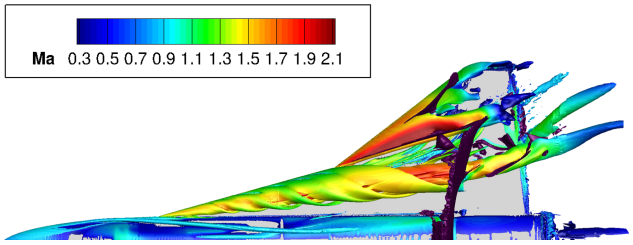

(a) $Ma = 0.85$, $\alpha = 16°$

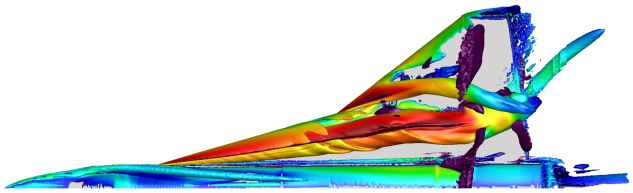

(b) $Ma = 0.85$, $\alpha = 24°$

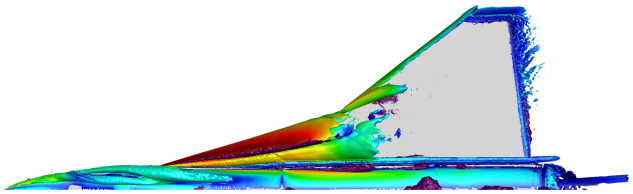

(c) $Ma = 0.85$, $\alpha = 32°$

FIG 11. Isosurfaces of the non-dimensional Q-Criterion of 50 for the double-delta-wing configuration at $Ma = 0.85$ & $Re = 1.20 \cdot 10^7$, $\alpha = 16°$, $24°$ and $32°$ & $\beta = 0°$.

vortex-shock interaction analysis for both double-delta and triple-delta-wing configurations.

4.4.1. Assessment of Numerical Results with Wind-Tunnel Data

Sideslip inflow conditions result in a decrease in the effective leading-edge sweep angle of the windward side. Consequently, the formation of the leading-edge vortices is expected to be more intense but less stable. Conversely, the leading-edge vortices feature diminished intensity but higher stability on the leeward side [30]. At $\alpha = 16°$, this trend is more evident in the numerical results as shown in Figure 12a and 12b.

Similar to the symmetric inflow computations, both simulations show higher suction levels induced by the IBV. Additionally, the strength of the first shock and its location are miscalculated by both methods. Yet, IDDES performs better regarding the attenuation of the suction footprint of the IBV. Experimental data reveal a more robust MBV development on the windward side, as seen in Figure 12c, whereas both numerical results predict a more intense MBV formation. On the other hand, numerical results predict a stronger shock, whereas wind-tunnel data reveal a gradual increase in pressure.

At $\alpha = 24°$, the flow field undergoes an abrupt change as indicated by the wind-tunnel data in Figure 13c. The onset of the vortex breakdown has already reached the apex on the windward side, while the vortex system is still present on the leeward side. This shows the influence of the effective leading-edge sweep angle on the stability of the vortex system. Due to the sideslip conditions, the lee side features a higher effective leading-edge sweep angle, enabling a more stable vortex system to develop. Numerical results capture the asymmetry in the pressure distribution; However, URANS shows that the IBV develops on the windward side, whereas IDDES represents the vortex breakdown on this side more accurately. Additionally, both results show higher suction levels on the starboard wing and overpredict the strength of the lee-side vortex system, as seen in Figure 13a and Figure 13b.

The experimental data illustrate the recovery of the surface pressure distribution at $\alpha = 32°$, as seen in Figure 14c. The IBV still develops partially on the leeward side, as accurately captured by IDDES, but the suction level is slightly overpredicted. On the other hand, the URANS result indicates a more stable IBV, which shows the deficiency of the URANS method at higher angles of attack.

4.4.2. Vortex-Shock Interactions

Figure 15 illustrates the formation of the shocks and leading-edge vortices for the triple-delta-wing configuration at $\alpha = 16°$ and $\alpha = 24°$ under sideslip conditions. The windward LEVs feature a larger cross-sectional area due to the sideslip conditions at $\alpha = 16°$. However, despite the high vortex intensity, both the IBV and the MBV undergo a significant reduction in local Ma upon encountering the second shock, indicating vortex breakdown. On the other hand, the leeward LEVs exhibit high stability, continuing to flow and displaying signs of interaction downstream of the trailing edge. At $\alpha = 24°$, the sudden upstream jump of the IBV breakdown on the starboard wing causes the suction levels to reduce significantly, as shown in the previous section. Accordingly, the absence of coherent $Q^* = 50$ isosurfaces indicates the early breakdown of both the IBV and the MBV. On the other hand, the leeward vortex system exhibits high stability, characterized by a high local Mach number over the entire wing section. The vortex-shock interaction on the leeward side does not weaken the vortices, and downstream of the trailing edge, the MBV and the IBV interact with each other. Besides, the forebody vortex deflects from the windward side across the fuselage toward the leeward side. Consequently, the significant change of the flow field on the windward side results in asymmetric lift generation on both sides, where the leeward side contributes more to the lift generation, resulting in a sign change of the rolling moment coefficient (C_{mx}) between $\alpha = 16°$ and $\alpha = 24°$, named as roll collapse.

For a complete comprehension of the flow field under the sideslip condition, the influence of the wing geometry is investigated, as well. Figure 16 shows the Q^* isosurfaces and shocks at $\alpha = 16°$ and $\alpha = 24°$ at $Ma = 0.85$ for the double-delta-wing configuration. At $\alpha = 16°$, the windward vortex system interacts with a stronger shock, which causes the MBV to burst, while the IBV remains firm after interacting with the shock, as shown in Figure 16a. On the leeward side, both vortices exhibit high local Ma values exceeding 1 after interacting with the shock, and vortex-vortex interaction is visible downstream of the trailing edge. At $\alpha = 24°$, the IBV development is depicted through the presence of $Q^* = 50$ isosurfaces, and its breakdown occurs downstream of the strake on the windward side, see Figure 15b. Yet, the MBV breaks down at an early stage, similar to the triple-delta wing configuration. On the leeward side, vortices show highly stable flow behavior with high local Ma values, showing no sign of vortex breakdown.

Lateral and directional aerodynamic coefficients are plotted in Figure 17, where diamonds and right triangles show the rolling moment (C_{mx}) and yawing moment (C_{mz}) co-

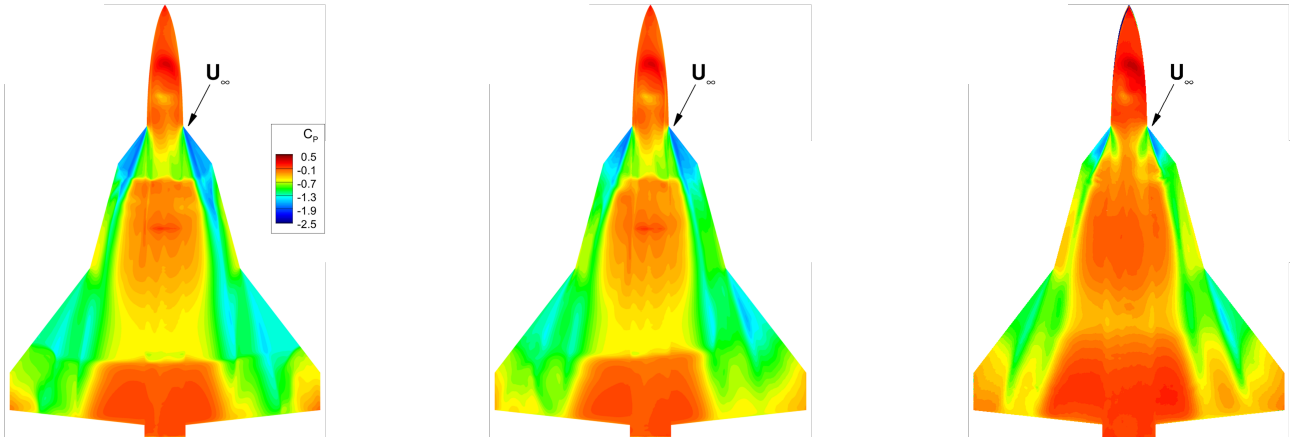

(a) URANS ($\alpha = 16°$) **(b) IDDES** ($\alpha = 16°$) **(c) WT Data** ($\alpha = 16°$)

FIG 12. Surface pressure distribution plots of the numerical results and the experimental data at $Ma = 0.85$ **&** $Re = 1.20 \cdot 10^7$**,** $\alpha = 16°$ **&** $\beta = 5°$**.**

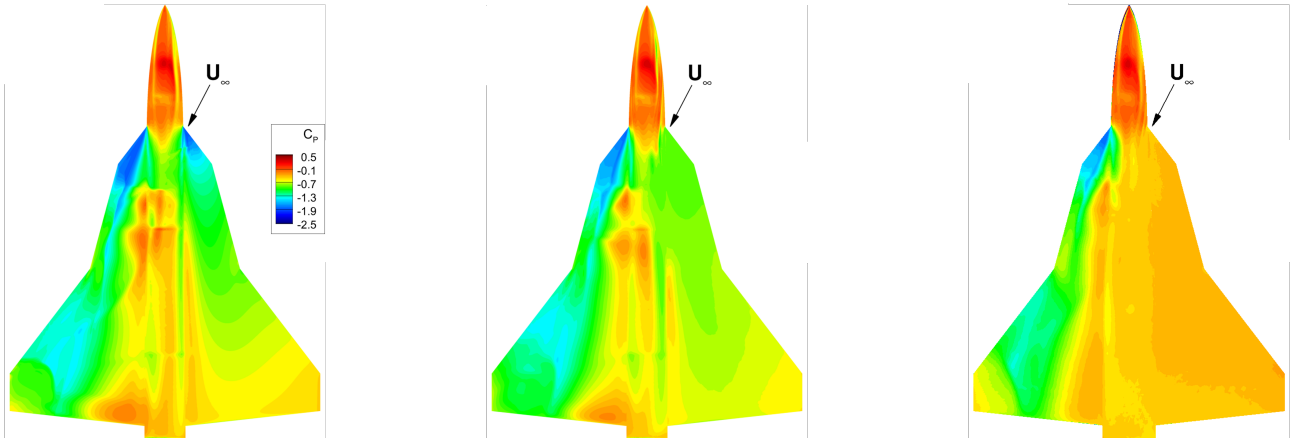

(a) URANS ($\alpha = 24°$) **(b) IDDES** ($\alpha = 24°$) **(c) WT Data** ($\alpha = 24°$)

FIG 13. Surface pressure distribution plots of the numerical results and the experimental data at $Ma = 0.85$ **&** $Re = 1.20 \cdot 10^7$**,** $\alpha = 24°$ **&** $\beta = 5°$**.**

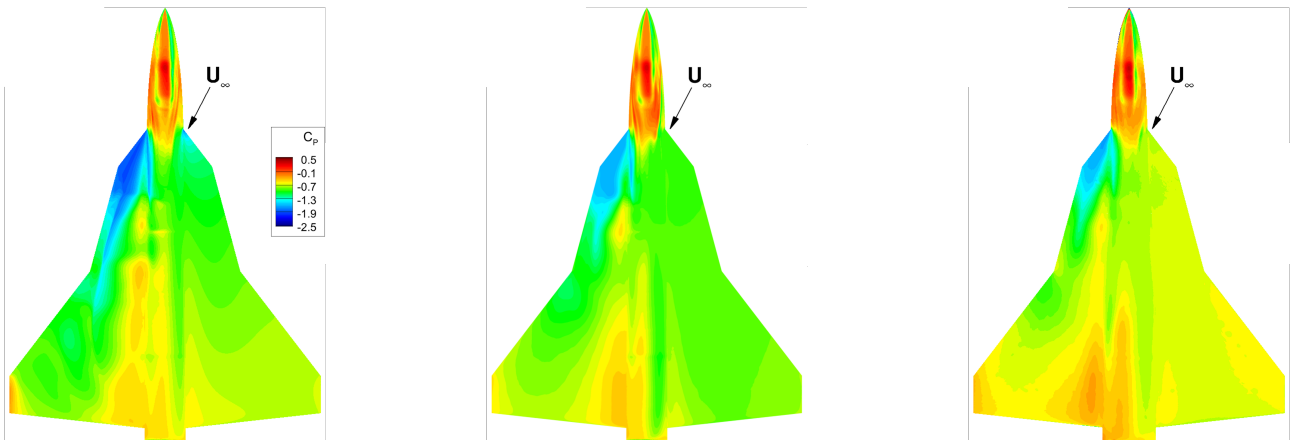

(a) URANS ($\alpha = 32°$) **(b) IDDES** ($\alpha = 32°$) **(c) WT Data** ($\alpha = 32°$)

FIG 14. Surface pressure distribution plots of the numerical results and the experimental data at $Ma = 0.85$ **&** $Re = 1.20 \cdot 10^7$**,** $\alpha = 32°$ **&** $\beta = 5°$**.**

efficients, respectively. C_{mx} is defined as positive for a downward rotation of the starboard wing. Experimental data reveal the roll collapse at $\alpha \approx 22°$, which begins to recover beyond $\alpha \approx 28°$ as the leeward-side vortices start to burst as well. IDDES captures the roll collapse and shows accurate results regarding lateral coefficients.

5. CONCLUSION

This study investigates the flow field around triple-delta-wing and double-delta-wing configurations with sharp leading edges, with a focus on vortex-vortex and vortex-shock interactions. Simulations were carried out using the DLR-TAU Code at Mach numbers $Ma = 0.75,\ 0.85,\ 0.95$ for an

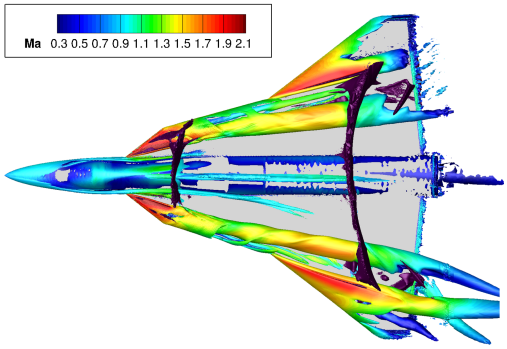

(a) $Ma = 0.85$, $\alpha = 16°$

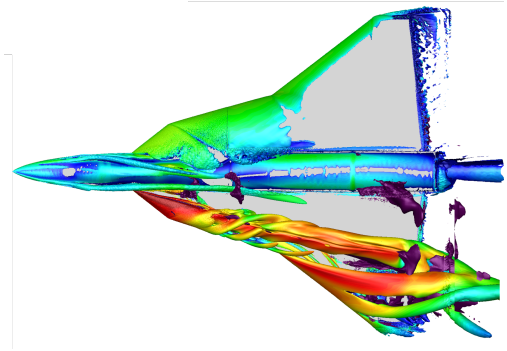

(b) $Ma = 0.85$, $\alpha = 24°$

FIG 15. Isosurfaces of the non-dimensional Q-Criterion of 50 for the triple-delta-wing configuration at $Ma = 0.85$ & $Re = 1.20 \cdot 10^7$, $\alpha = 16°$ and $24°$ & $\beta = 5°$.

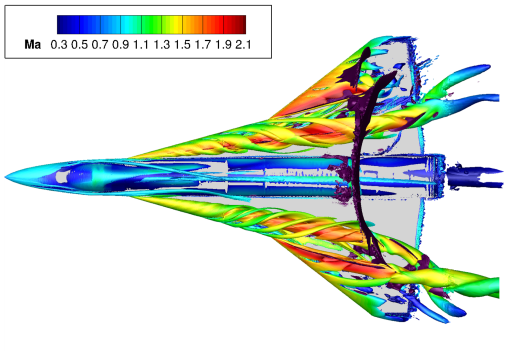

(a) $Ma = 0.85$, $\alpha = 16°$

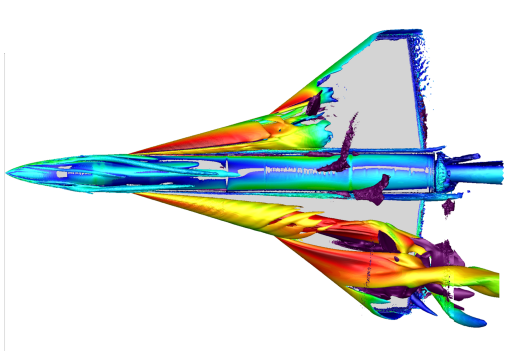

(b) $Ma = 0.85$, $\alpha = 24°$

FIG 16. Isosurfaces of the non-dimensional Q-Criterion of 50 for the double-delta-wing configuration at $Ma = 0.85$ & $Re = 1.20 \cdot 10^7$, $\alpha = 16°$ and $24°$ & $\beta = 5°$.

angle of attack range of $16° \leq \alpha \leq 32°$ with $4°$ and $8°$ increments for URANS and Improved Delayed Detached Eddy Simulation (IDDES) computations, respectively. Both

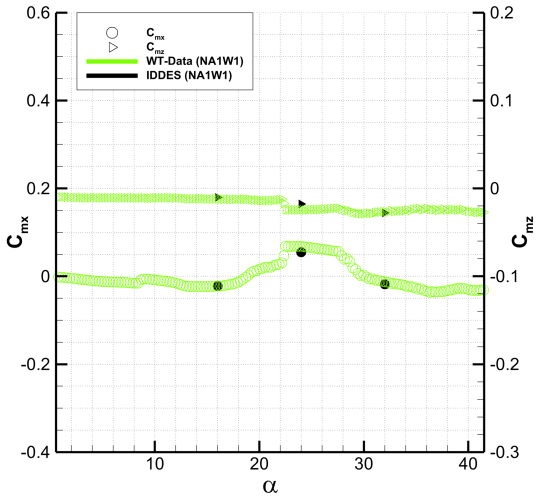

FIG 17. Lateral and Directional Aerodynamic Coefficients at $\beta = 5°$.

symmetric and asymmetric flow conditions were analyzed by setting the angle of sideslip β to $0°$ and $5°$, respectively. A time-step sensitivity study demonstrated that a physical time-step size $\Delta t = 2 \cdot 10^{-5}\,\mathrm{s}$ provides the best compromise between accuracy and the computational cost. The numerical results were compared with the wind tunnel data provided by DLR and Airbus Defence and Space. At high incidence angles, URANS fails to capture the flow field, predicting the formation of the Inboard Vortex (IBV) at $\alpha = 32°$, whereas wind tunnel data and IDDES results indicate that the vortex breakdown has reached the apex. For $\beta = 0°$, the influence of Mach number, angle of attack, and wing geometry is investigated. The vortex topology becomes flatter with increasing Ma, while the secondary vortex formation becomes more pronounced with decreasing Ma. For all Ma cases, the distortion of the secondary vortex is observed downstream of the leading-edge vortex controller (LEVCON), which is intensified by increasing Ma. Vortex core data are extracted to compute the Rossby number (Ro), and the axial velocity deficit (δ) in order to determine the breakdown characteristics. The location of the IBV breakdown moves downstream with increasing Ma, namely $x/c_r = 0.75$ for $Ma = 0.75$ and $x/c_r = 0.86$ for $Ma = 0.95$, while the IBV undergoes a shock-induced vortex breakdown at around $x/c_r = 0.77$ at $Ma = 0.85$. The Midboard Vortex (MBV) breakdown is not observed for any Ma case. For the triple-delta-wing configuration, the effect of the angle of attack is analyzed at $Ma = 0.85$ for angles of attack of $\alpha = 24°$ and $32°$. The IBV develops more intensely at $\alpha = 24°$ than at $\alpha = 16°$, yet it is more susceptible to vortex breakdown, bursting at $x/c_r = 0.67$. Vortex breakdown is associated with a drop in Ro below the stability threshold for all cases. At $\alpha = 32°$, vortex breakdown has already reached the apex; consequently, neither the IBV nor the MBV develops. The influence of the wing geometry is examined at $Ma = 0.85$. Accordingly, the double-delta wing features a more stable IBV, which does not burst at $\alpha = 16°$ and $24°$ over the wing despite its interaction with the shock, whereas the MBV is impacted more through the shock. In contrast to the triple-delta-wing configuration, the IBV formation remains present on the double-delta-wing configuration at $\alpha = 32°$.

Under sideslip conditions at $Ma = 0.85$, the windward-side vortex system is more intense at $\alpha = 16°$; however, the interaction with the second shock significantly decelerates the IBV and the MBV, causing breakdown. Meanwhile, the

leeward-side vortex system is still present downstream of the trailing edge. Roll collapse occurs for both configurations between $\alpha = 16^\circ$ and 24° as the windward-side vortex system breaks down; consequently, asymmetric lift generation on both wings leads to roll instability. The roll behavior is recovered with an increase in the incidence angle, as the vortex breakdown also starts to occur on the leeward side. IDDES computations accurately capture the lateral aerodynamic coefficients, including the onset of the roll reversal. Further investigations will examine the impact of leading-edge radius and Reynolds number on the formation of the leading-edge vortex system and vortex interactions at various transonic speeds.

ACKNOWLEDGMENTS

The authors gratefully acknowledge the funding of the project by the Deutsche Forschungsgemeinschaft (DFG, German Research Foundation) – project number DFG BR1511/13-2. The DLR is appreciated for providing the flow simulation software DLR TAU Code. Additionally, both DLR and Airbus Defence and Space are acknowledged for the provision of experimental data, utilized for comparative analysis with the numerical results in this study. The authors also thank the Gauss Center for Supercomputing e.V. for funding this project by providing computing time at the Leibniz Supercomputing Center (LRZ, www.lrz.de).

Contact address:

yasin.oezdemir@tum.de

References

[1] Hitzel, S. M. Sub- and transonic vortex breakdown flight condition simulations of the f-16xl aircraft. *Journal of Aircraft*, 54(2):428–443, 2017. DOI: 10.2514/1.C033246.

[2] Breitsamter, C. Unsteady flow phenomena associated with leading-edge vortices. *Progress in Aerospace Sciences*, 44(1):48–65, 2008. ISSN: 0376-0421. DOI: https://doi.org/10.1016/j.paerosci.2007.10.002.

[3] Delery, J. Aspects of vortex breakdown. *Progress in Aerospace Sciences*, 30(1):1–59, 1994. ISSN: 0376-0421. DOI: https://doi.org/10.1016/0376-0421(94)90002-7.

[4] Pfnür, S., Breitsamter, C. Leading-edge vortex interactions at a generic multiple swept-wing aircraft configuration. *Journal of Aircraft*, 56(6):2093–2107, 2019. DOI: 10.2514/1.C035491.

[5] Sedlacek, D., Breitsamter, C., Visonneau, M.,Guilmineau, E., Jeroen Wackers, J. *Assessment of Hybrid Delta Wing Vortex Flow Investigation – Part I at Subsonic Conditions*. DOI: 10.2514/6.2022-0565.

[6] Sedlacek, D., Biechele, S., Breitsamter, C. Numerical investigations of vortex formation on a generic multiple-swept-wing configuration. *CEAS Aeronautical Journal*, 13:295–310, 1 2022. ISSN: 18695590. DOI: 10.1007/s13272-021-00566-y.

[7] Sedlacek, D., Kasi, A., Breitsamter, C. Influence of the leading-edge radius on vortex development at hybrid-delta-wing configurations. In *10th European Conference for Aeronautics and Space Sciences (EUCASS)*, 2023. Published online by the EUCASS association. DOI: 10.13009/EUCASS2023-418.

[8] Drougge, G. The international vortex flow experiment for computer code validation. In *ICAS Proceedings*, volume 1, pages XXXV–XLI, Jerusalem, 1988.

[9] Hummel, D. The second international vortex flow experiment (vfe-2): Results of the first phase 2003–2008. In *Proceedings of the 26th International Congress of the Aeronautical Sciences (ICAS)*, ICAS, 2008. Paper 057.

[10] Schiavetta, L., Boelens, O., Crippa, S., Cummings, R., Fritz, W., Badcock, K. *Shock Effects on Delta Wing Vortex Breakdown*. DOI: 10.2514/6.2008-395.

[11] Rizzi, A., Boelens, O., Jirasek, A., Badcock, K. *What Was Learned from Numerical Simulations of F-16XL (CAWAPI) at Flight Conditions*. DOI: 10.2514/6.2007-683.

[12] Russell, A., Werner, M., Peshkin, D., Eccleston, S. P. *Assessment of Hybrid Delta Wing Vortex Flow Investigation – Part II at Transonic Conditions*. DOI: 10.2514/6.2022-0158.

[13] Werner, M., Schütte, A., Weiss, S. *Turbulence Model Effects on the Prediction of Transonic Vortex Interaction on a Multi-Swept Delta Wing*. DOI: 10.2514/6.2022-0295.

[14] Hövelmann, A., Pölzlbauer, P., Pfnür, S., Winkler, A., M. Hitzel, S. M. *Hybrid-Delta Wing Simulations – Industrial Application for Combat Aircraft Design*. DOI: 10.2514/6.2022-0157.

[15] Werner, M., M. Rein, M., Richter, K., Weiss, S. Experimental and Numerical Analysis of the Aerodynamics and Vortex Interactions on Multi-Swept Delta Wings. *CEAS Aeronautical Journal*, 14:927–938, 10 2023. ISSN: 18695590. DOI: 10.1007/s13272-023-00678-7.

[16] Di Fabbio, T., Tangermann, E., Klein, M. Analysis of the Vortex-Dominated Flow Field over a Delta Wing at Transonic Speed. *The Aeronautical Journal*, 127:1851–1868, 11 2023. ISSN: 0001-9240. DOI: 10.1017/aer.2023.30.

[17] Di Fabbio, T., Tangermann, E., Klein, M. Flow Pattern Analysis on a Delta Wing at Transonic Speed. *AIAA Science and Technology Forum and Exposition, AIAA SciTech Forum 2022*, 2022. DOI: 10.2514/6.2022-1204.

[18] Di Fabbio, T., Rajkumar, K., Tangermann, E., Klein, M. Towards the Understanding of Vortex Breakdown for Improved RANS Turbulence Modeling. *Aerospace Science and Technology*, 146, 3 2024. ISSN: 12709638. DOI: 10.1016/j.ast.2024.108973.

[19] Sedlacek, D. *Aerodynamics of Interfering Vortex Systems at Generic Hybrid Delta-Wing Configurations*. PhD thesis, Technische Universität München, 2025. https://mediatum.ub.tum.de/1782515.

[20] Spalart, P., Allmaras, S. *A one-equation turbulence model for aerodynamic flows*. DOI: 10.2514/6.1992-439.

[21] Allmaras, S., Forrester, J., Spalart, P. Modifications and clarifications for the implementation of the spalart-allmaras turbulence model. *Seventh International Conference on Computational Fluid Dynamics (ICCFD7)*, pages 1–11, 01 2012.

[22] Shur, M., Strelets, M., Travin, A., P. Spalart, P. Turbulence Modeling in Rotating and Curved Channels: Assessing the Spalart-Shur Correction. *AIAA Journal*, 38(5):784–792, 2000. DOI: 10.2514/2.1058.

[23] Spalart, P., Jou, W. H., Strelets, M., Allmaras, S. Comments on the feasibility of les for wings, and on a hybrid rans/les approach. 01 1997.

[24] Spalart, P., Deck, S., Shur, M., Squires, K., Strelets, M., Travin, A. A New Version of Detached-Eddy Simulation, Resistant to Ambiguous Grid Densities. *Theoretical and Computational Fluid Dynamics*, 20:181–195, 7 2006. ISSN: 09354964. DOI: 10.1007/s00162-006-0015-0.

[25] Shur, M. L., Spalart, P. R., Strelets, M., Travin, A. A Hybrid RANS-LES Approach with Delayed-DES and Wall-Modelled LES Capabilities. *International Journal of Heat and Fluid Flow*, 29:1638–1649, 12 2008. ISSN: 0142727X. DOI: 10.1016/j.ijheatfluidflow.2008.07.001.

[26] Schiavetta, L., Badcock, K., Cummings, R. *Comparison of DES and URANS for Unsteady Vortical Flows over Delta Wings*. DOI: 10.2514/6.2007-1085.

[27] Kolář, V. Vortex Identification: New Requirements and Limitations. *International Journal of Heat and Fluid Flow*, 28(4):638–652, 2007. ISSN: 0142-727X. Including Special Issue of Conference on Modelling Fluid Flow. DOI: https://doi.org/10.1016/j.ijheatfluidflow.2007.03.004.

[28] Tecplot, Inc., Bellevue, WA, USA. *Tecplot 360 EX 2018 Release 2 User's Manual*, 2018. Version 2018 R2.

[29] Robinson, B.A., Barnett, R. M., Agrawal, S. Simple Numerical Criterion for Vortex Breakdown. *AIAA Journal*, 32:116–122, 1994. ISSN: 00011452. DOI: 10.2514/3.11958.

[30] Hövelmann, A., Winkler, A., Hitzel, S., Richter, K., Werner, M. Analysis of vortex flow phenomena on generic delta wing planforms at transonic speeds. In *21st STAB/DGLR Symposium on New Results in Numerical and Experimental Fluid Mechanics*, volume 142 of *Notes on Numerical Fluid Mechanics and Multidisciplinary Design*, pages 307–316. Springer Nature, 2020. Print ISBN 978-3-030-25252-6 Online ISBN 978-3-030-25253-3 ISSN-electronic 1860-0824.